# VELOCITY DISPERSION OF IONIZED GAS AND MULTIPLE SUPERNOVA EXPLOSIONS

E. O. Vasiliev<sup>1,2,3</sup>, A. V. Moiseev<sup>3,4</sup> and Yu. A. Shchekinov<sup>2</sup>

- <sup>1</sup> Institute of Physics, Southern Federal University, Stachki Ave. 194, Rostov-on-Don, 344090 Russia; eugstar@mail.ru
- Department of Physics, Southern Federal University, Sorge Str. 5, Rostov-on-Don, 344090 Russia
- Special Astrophysical Observatory, Russian Academy of Sciences, Nizhnij Arkhyz, Karachaevo-Cherkesskaya Republic, 369167 Russia
- <sup>4</sup> Sternberg Astronomical Institute, Moscow M. V. Lomonosov State University, Universitetskij pr. 13, 119992 Moscow, Russia

Received: 2015 March 25; accepted: 2015 April 20

**Abstract.** We use 3D numerical simulations to study the evolution of the  ${\rm H}\alpha$  intensity and velocity dispersion for single and multiple supernova (SN) explosions. We find that the  $I_{{\rm H}\alpha}$ –  $\sigma$  diagram obtained for simulated gas flows is similar in shape to that observed in dwarf galaxies. We conclude that colliding SN shells with significant difference in age are responsible for high velocity dispersion that reaches up to  $\gtrsim 100~{\rm km\,s^{-1}}$ . Such a high velocity dispersion could be hardly obtained for a single SN remnant. Peaks of velocity dispersion in the  $I_{{\rm H}\alpha}$ –  $\sigma$  diagram may correspond to several isolated or merged SN remnants with moderately different ages. Degrading the spatial resolution in the  ${\rm H}\alpha$  intensity and velocity dispersion maps makes the simulated  $I_{{\rm H}\alpha}$ –  $\sigma$  diagrams close to those observed in dwarf galaxies not only in shape, but also quantitatively.

**Key words:** galaxies: ISM – ISM: bubbles – ISM: supernova remnants – ISM: kinematics and dynamics – shock waves – methods: numerical

### 1. INTRODUCTION

3D spectroscopy in optical emission lines yields detailed information about the kinematics of the ionized gas in the interstellar medium (ISM) of external galaxies with a seeing-limited angular resolution. On the one hand, it provides an angular resolution of 1-3 arcsec, which is an order of magnitude higher than that achieved in radio observations. However, on the other hand, it is limited only to the regions around ionizing radiation sources like OB stars, stellar winds, and supernova explosions. Kinetic energy output from these objects may be responsible for driving turbulent motions in ambient gas and forming galactic outflows. The observed characteristic of these motions is velocity dispersion  $\sigma$  defined as the standard deviation of the Gaussian profile describing Balmer emission lines after accounting for the instrumental effects and subtracting the contribution of natural and thermal broadening in the HII regions. To interpret observations of star-forming

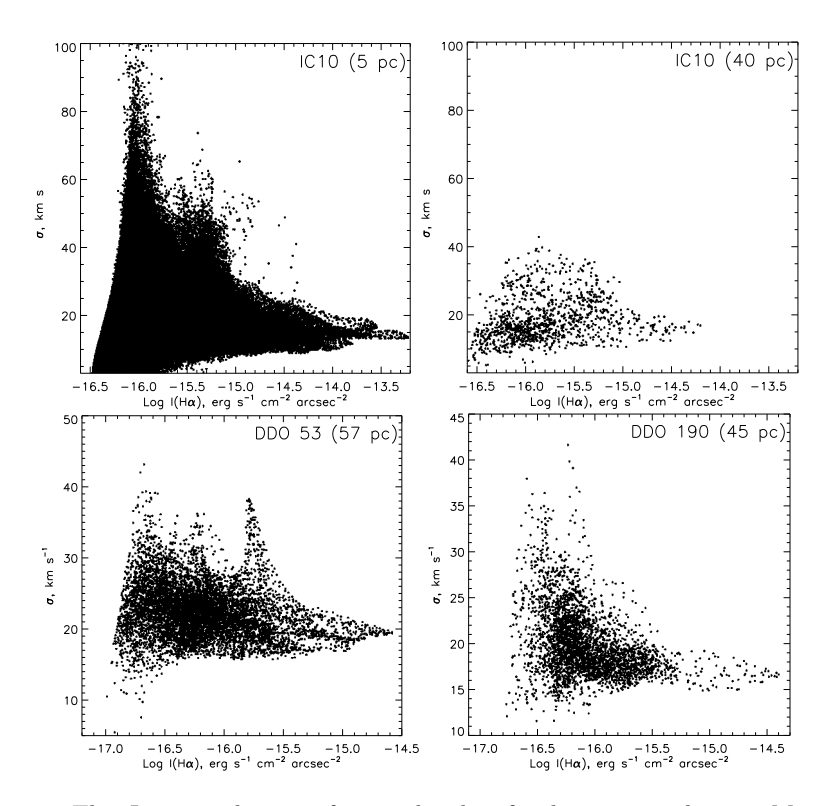


**Fig. 1.** The  $I_{\rm H\alpha}-\sigma$  diagram for nearby dwarf galaxies according to Moiseev & Lozinskaya (2012): IC 10 (original and smoothed data), DDO 53 and DDO 190. The spatial resolution is indicated in the brackets.

complexes Muñoz-Tuñón et al. (1996) and Yang et al. (1996) have proposed to use the relation between the  $H\alpha$  intensity (i.e. the emission line surface brightness) and velocity dispersion – the  $I_{\rm H\alpha}$ – $\sigma$  diagram. More recently, Martínez-Delgado et al. (2007), Bordalo et al. (2009), Moiseev et al. (2010), Moiseev & Lozinskaya (2012) used  $I_{\rm H\alpha}$ - $\sigma$  diagrams to study ionized gas in several dwarf galaxies. Fig. 1 shows such diagrams for the nearby dwarf irregular galaxies IC 10, DDO 190 and DDO 53. Observational data for these diagrams were obtained using a scanning Fabry-Perot interferometer with the 6-m telescope of the SAO RAS and are described in detail by Moiseev & Lozinskaya (2012). The spatial resolution of the observations of the nearest galaxy IC 10 (5 pc) is eight times better than that for the DDO 190 and DDO 53 galaxies. In low-resolution observations, gaseous motions in small HII regions, thin shells, and colliding shocks are averaged with neighboring low-velocity flows. As a result, the data on the small-scale kinematics of gas is lost for the two latter galaxies that are more distant than IC 10. To imitate the effect of low resolution, the original data cube for IC 10 was first smoothed by the two-dimensional Gaussians, and then binned to make the resulting spatial resolution and sampling comparable to those for DDO 190 and DDO 53 (Moiseev & Lozinskaya 2012). With resolution so degraded the diagram for IC 10 looks similar to these for DDO 190 and DDO 53 and fills the same range of  $\sigma$ . In general, all such diagrams have similar shape, because there are several main

sources that contribute to the H $\alpha$  line intensity and that drive motions in turbulent ISM. Namely, there are H II regions, stellar winds, and supernova remnants. Acting together, they form a multiphase turbulent ISM. So far, only quantitative interpretation of  $I_{\rm H}\alpha^ \sigma$  diagrams was proposed by Muñoz-Tuñón et al. (1996). However, one can be interested in how ionized gas has reached to the state, which corresponds to the shape of  $I_{\rm H}\alpha^ \sigma$  diagrams observed in galaxies.

In this note we consider the evolution of the  $H\alpha$  intensity and velocity dispersion for single and multiple supernova explosions.

#### 2. NUMERICAL MODEL

We are interested in the relation between emissivity in the H $\alpha$  line and velocity dispersion for gaseous flows driven by multiple SN explosions in star-forming galaxies (for a detailed study of multiple SNe dynamics, see Vasiliev et al. 2015). We follow the evolution of the H $\alpha$  emission intensity and velocity dispersion in a small box of 200 pc<sup>3</sup>. We consider a finite number of SNe exploding every 10<sup>5</sup> and 10<sup>4</sup> yrs, which corresponds to the SN rate of  $1.25 \times 10^{-12}$  and  $1.25 \times 10^{-11}$  pc<sup>-3</sup> Myr<sup>-1</sup> in the case of continuous star formation on galactic scales. For comparison, we investigate how the corresponding quantities evolve in the case of a single SN explosion.

We carry out 3-D hydrodynamic simulations (Cartesian geometry) of multiple/single SNe explosions. We adopt periodic boundary conditions. The computational domain has the size of  $200^3$  pc<sup>3</sup> and is partitioned into  $300^3$  cells, corresponding to a physical cell size of 0.75 pc. We consider the background number density values of 0.1 and  $1~\rm cm^{-3}$ , and the adopted background temperature is  $10^4$  K. Metallicity is constant within the computational domain (we do not address here the mixing of metals ejected by SNe and plan to explore this issue in a separate study), and we consider the cases with  $Z=0.1, 1~\rm Z_{\odot}$ . We inject the energy of each SN in the form of thermal energy in a region of radius  $r_i=1.5$  pc. The energy of each SN equals  $10^{51}$  erg. SNe are distributed uniformly and randomly throughout the computational domain.

We use three-dimensional unsplit total variation diminishing (TVD) code based on the Monotonic Upstream-Centered Scheme for Conservation Laws (the MUSCL-Hancock scheme) and the Haarten-Lax-van Leer-Contact (HLLC) method (e.g., Toro 1999) as approximate Riemann solver. This code has successfully passed the whole set of tests proposed in Klingenberg et al. (2007).

In the energy equation we take into account cooling processes, adopting the tabulated non-equilibrium cooling curve (Vasiliev 2013). This cooling rate is obtained for a gas cooled isobarically from  $10^8$  down to 10 K. The full description of our method of cooling rate calculations and the references to the atomic data can be found in Vasiliev (2011, 2013). Briefly, the non-equilibrium calculation includes the ionization kinetics of all ionization states for the following chemical elements: H, He, C, N, O, Ne, Mg, Si, Fe, as well as molecular hydrogen kinetics at  $T < 10^4$  K. The heating rate is adopted to be constant and chosen so that the background gas would not cool. Stability is lost when density and temperature go beyond the narrow range near the equilibrium state.

We use the pre-computed cooling rates because self-consistent calculation of cooling rates in multi-dimensional dynamics is a very time consuming task. In general, the evolution of gas behind shocks with velocities higher than  $\gtrsim 150~{\rm km\,s^{-1}}$ 

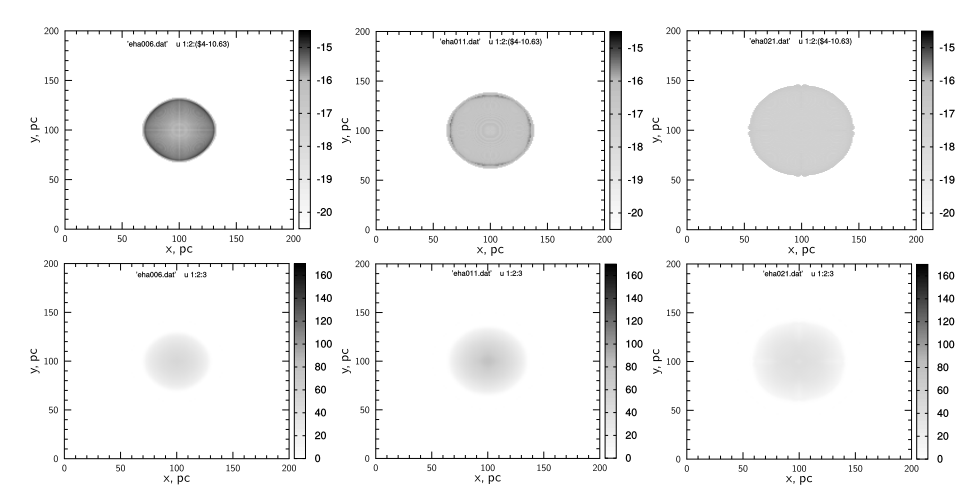


**Fig. 2.** H $\alpha$  intensity  $I_{\text{H}\alpha}$  (in erg cm<sup>-2</sup> s<sup>-1</sup> arcsec<sup>-2</sup>) (the top row) and velocity dispersion (in km s<sup>-1</sup>) (the bottom row) maps for a single SN explosion at t = 0.1, 0.2 and 0.4 Myr (from left to right).

is very close to that of gas cooled from very high temperature,  $T=10^8\,\mathrm{K}$  (e.g., Vasiliev 2012). Here we study multiple SN explosions whose shells collide and merge with each other with typical velocities higher than  $100~\mathrm{km\,s^{-1}}$ . The non-equilibrium cooling rates can therefore be pre-computed for a gas cooled from very high temperature, e.g.  $T=10^8\,\mathrm{K}$ , and these rates can be used to study SN shell evolution in tabulated form. We follow ionization kinetics of the most abundant chemical elements, and therefore we know the fractions of all ionic states of these elements. These fractions are used then in simulations in tabulated form. To calculate the line-of-sight  $\mathrm{H}\alpha$  intensity we use the  $\mathrm{H}\alpha$  volume emissivity of a gas parcel (e.g., Kaplan & Pikelner 1979). Gas layers with high temperature (inside SN ejecta) produce small numbers of  $\mathrm{H}\alpha$  photons (because of the small number of recombinations), while radiatively cooled gas in the SN shell is the dominant contributor to the  $\mathrm{H}\alpha$  intensity. Velocity dispersion reflects the kinematics of gaseous flows along sight lines.

# 3. RESULTS

First of all, to understand  $H\alpha$  emission and velocity dispersion distributions for multi-SNe explosions, we consider these distributions for single SNe exploded in homogeneous medium. Fig. 2 shows the  $H\alpha$  intensity and velocity dispersion maps for three time instants. The average intensity can be seen to drop with time, and note that velocity dispersion in the direction of the explosion center grows at  $t \sim 0.2$  Myr and then decreases. Around  $t \sim 0.2$  Myr, the reverse shock overtakes the blastwave due to the deceleration of the latter. Because of higher velocity of the reverse shock, velocity dispersion increases. After short interaction between shocks, dispersion drops monotonically in time. Fig. 3 shows the  $I_{H\alpha} - \sigma$  diagram for a single SN explosion. It can be clearly seen that the locus of points corresponding to the same time instant shifts with time to the region with lower  $H\alpha$  intensity. Velocity dispersion reaches its maximum of about 80 km s<sup>-1</sup> when the reverse shock is close to the blastwave. The intensity and velocity dispersion

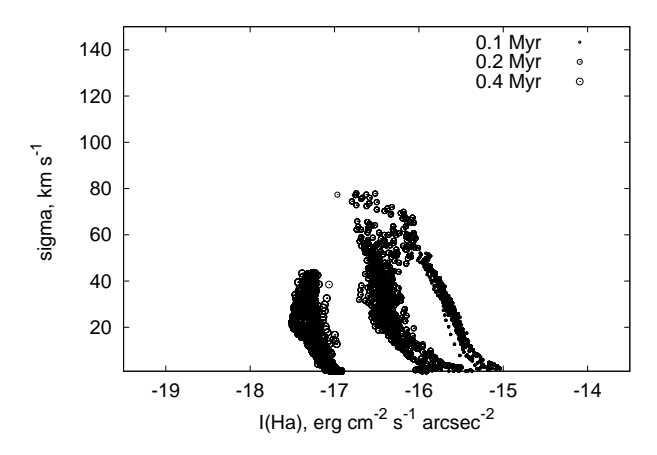
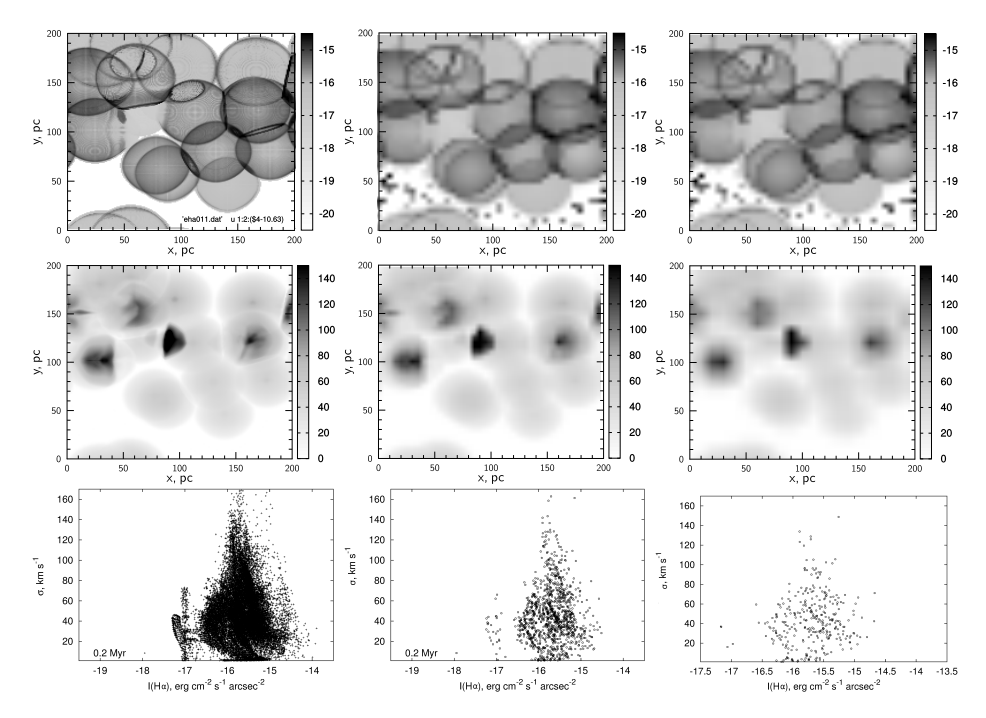


**Fig. 3.** The  $I_{\text{H}\alpha}$  –  $\sigma$  diagram for a single SN explosion at  $t=0.1,\ 0.2$  and 0.4 Myr (from small to large symbols).

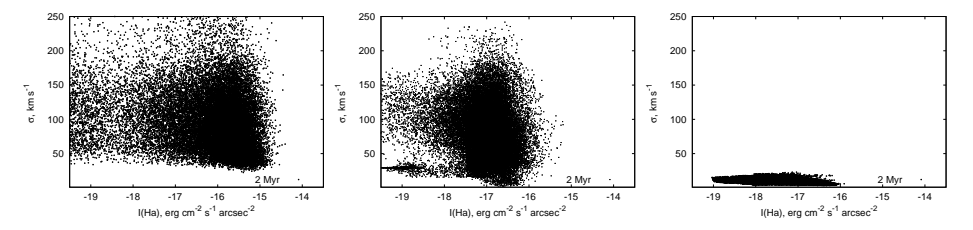
become smaller for older remnant. The decrease of the ambient density leads to longer evolution, but the maximum velocity dispersion after the beginning of the radiation phase depends only slightly on the ambient density.

Fig. 4 (the left-column panels) shows the  $H\alpha$  intensity (the upper row) and velocity dispersion (the middle row) maps and the  $I_{\text{H}\alpha}$ – $\sigma$  diagram (bottom) for the SN rate  $1.25 \times 10^{-11} \text{ pc}^{-3} \text{Myr}^{-1}$  at t=0.2 Myr. Several SN bubbles are clearly identified (only two dozen SNe have exploded till this time), some of them interact with each other. It can be clearly seen that high  $H\alpha$  intensity and velocity dispersion are associated with young SN remnants. However, the highest velocity dispersion can be found around colliding shells of young and old SNe. A breakthrough of high velocity gas of young SN shell into warm rarefied interiors of the old SN produces a strong shock wave. We can thus conclude that collisions of SN shells with significant difference in age are responsible for the velocity dispersion rising as high as  $\gtrsim 100 \text{ km s}^{-1}$ . When two SN shells of similar age collide, a cold layer with divergent shocks forms, in this case the velocity dispersion does not increase significantly. Several peaks of  $\sigma$  in the diagram correspond to multiple stand-alone SN remnants with moderately different ages. Similar peaks can be found in the dwarf galaxy DDO 53 (see Fig. 1). For instance, a similar pattern occurs at  $t \sim (3-5) \times 10^5$  yrs for SN explosions with frequency 1 per  $10^5$  yr, whose shells do not interact each other (or interact only slightly).

One can see that the form of the  $I_{\rm H\alpha}$ – $\sigma$  diagram is similar to that observed in dwarf galaxies after 10–20 SN explosions (several of them should collide with each other) with a frequency of 1 explosion per  $\sim 10^4$  yr. The decrease of the frequency (or, in general, SN rate) leads to lower velocity dispersion. Later in time the form of the  $I_{\rm H\alpha}$ – $\sigma$  diagram depends on whether SN explosions continue or cease. In the first case, SN shell collisions lead to further increase of velocity dispersion, which can reach  $\sim 200-250~{\rm km\,s^{-1}}$  (Fig. 5, the left and middle panels). Both rarefied and hot gas has high velocity dispersion, but low H $\alpha$  intensity. Note that, because the observed  $\sigma$  maps are masked by the fixed S/N level (the left-hand side boundary of the point cloud in the observed diagrams is due to such masking), such rarefied and hot gas cannot be detected in observations. The decrease of SN frequency shifts the point cloud toward lower intensities (Fig. 5, the middle panel). For the



**Fig. 4.** H $\alpha$  intensity  $I_{\rm H}\alpha$  (in erg cm<sup>-2</sup> s<sup>-1</sup> arcsec<sup>-2</sup>) (the top row) and velocity dispersion (in km s<sup>-1</sup>) (the middle row) maps and the  $I_{\rm H}\alpha$ - $\sigma$  diagram (the bottom row) for the SN rate  $1.25\times 10^{-11}~{\rm pc^{-3}\,Myr^{-1}}$  at t=0.2 Myr. The left-column panels show the numerical data without degrading the resolution. The middle-column panels show the smoothed and binned data for h=2.5 pc and N=5 pc and the right-column panels, the smoothed and binned data for h=5 pc and N=10 pc.



**Fig. 5.** The  $I_{\rm H\alpha}$   $^-\sigma$  diagrams for continuous SN explosions with a rate of  $1.25 \times 10^{-11}~{\rm pc}^{-3}~{\rm Myr}^{-1}$  (1 SN per  $10^4~{\rm yrs}$  in a 200 pc<sup>3</sup> box, the left panel),  $1.25 \times 10^{-12}~{\rm pc}^{-3}~{\rm Myr}^{-1}$  (1 SN per  $10^5~{\rm yrs}$  in a 200 pc<sup>3</sup> box, the middle panel) and for a limited (15) number of SNe exploding with a delay of  $10^4~{\rm yrs}$  (the right panel) at  $t=2~{\rm Myr}$ .

case of limited SN number, the SN shells lose their energy during  $\sim 1$  Myr (in gas with  $n=0.1~{\rm cm}^{-3}$ ) after the last SN has exploded, thus, both H $\alpha$  intensity and velocity dispersion drop to negligible values (Fig. 5, right panel).

Thus, the  $I_{\rm H\alpha}-\sigma$  diagram obtained in our simulations is expected to be close to the observed one if (i) a star-formation burst leads to 10–20 nearest SN explosions, (ii) several SN shells collide, and (iii) the next burst does not occur before

previous SN remnants cool down and merge with the ISM. Note that the form of the computed diagram is similar to the observed diagram only several hundred thousand years after the burst has finished, and hence we can conclude that the last star-formation episode in the observed galaxies with similar-shaped diagrams should have occurred no earlier than several hundred thousand years ago.

In actual observations the spatial resolution is much lower than that in our simulations. To test our conclusions and compare our results with observations we degrade the resolution of the H\$\alpha\$ and velocity dispersion maps. We smooth the maps with a 2D Gaussian filter of \$h\$ size and then re-bin the smoothed maps with a bin size equal to \$N\$. Fig. 4 (the middle- and right-column panels) shows the H\$\alpha\$ intensity and the velocity dispersion after the degrading procedure. The maximum of velocity dispersion decreases from  $\sim 160-170~{\rm km\,s^{-1}}$  in the original map down to  $\sim 120-140~{\rm km\,s^{-1}}$  for \$h=5\$ pc and \$N=5\$ pc\$ (the middle column) and down to  $\sim 100-110~{\rm km\,s^{-1}}$  for \$h=10\$ pc and \$N=10\$ pc (the right column). The spatial resolution of the degraded maps is close to that in the actual observations of IC 10. Thus the velocity dispersion peak in the degraded \$I\_{\rm H}\alpha - \sigma\$ diagrams has a magnitude similar to that observed in dwarf galaxies (Martínez-Delgado et al. 2007; Moiseev et al. 2010; Moiseev & Lozinskaya 2012), and the model data points occupy similar ranges of Balmer lines surface brightness and line-of-sight velocity dispersion.

Typical sizes of the  $H\alpha$  emitting regions are about one kiloparsec in the dwarf galaxies considered, and so the periodic boundary conditions adopted for the box 200 pc<sup>3</sup> look quite consistent with the real situation. Indeed, for a sufficiently high rate of supernovae the shells from different explosions may collide with each other many times inside such a volume and form collective bubbles. This picture is similar to that simulated in our models. Periodic boundary conditions mimic a uniform distribution of star formation rate in a larger volume periodically reproduced by our single computational domain, and by no means result in an overestimate of the star formation rate and velocity dispersion. Velocity dispersion is determined by the gas layer with the highest velocity along a line of sight. For a superbubble this value corresponds to the free expansion velocity of the outer shell, whereas for multiple collisions of SNe their shells can suppress each other, so that the velocity dispersion for gas in shells may be lower than that for a well-developed superbubble. A SN explosion inside the rarefied interior of a bubble increases the velocity dispersion, however this gas has extremely high temperature and does contribute to  $H\alpha$  emission. As is evident from Fig. 4, SN shells do not occupy the whole volume at t = 0.2 Myr, and the shape of the  $I_{\text{H}\alpha}$ - $\sigma$  diagram is very similar to the observed one. During further evolution SNe explode in hot gas, velocity dispersion increases (see the two left panels in Fig. 5), but  $H\alpha$  emission from high velocity dispersion gas is low. As a result, the diagram broadens towards lower emissivity and higher dispersion. Furthermore, note that reduced spatial resolution in observations results in an underestimate of the inferred velocity dispersion.

# 4. CONCLUSIONS

We studied the  $H\alpha$  intensity – velocity dispersion diagram for single and multiple SNe. We found that the diagrams obtained in our simulations are close in shape to those observed in the nearby dwarf galaxies. For a single SN remnant, velocity dispersion reaches its maximum, of about several dozen km s<sup>-1</sup>, when the reverse shock is close to the blastwave. We conclude that collisions of SN

shells with significant difference in age are responsible for high velocity dispersion which reaches the values  $\gtrsim 100~\rm km\,s^{-1}$ . Peaks of velocity dispersion in the  $I_{\rm H\alpha}$ – $\sigma$  diagram may correspond to several stand-alone or merged SN remnants with moderately different ages. Similar structures can be found in the diagrams for the dwarf galaxy DDO 53. We investigated the effect of decreasing the spatial resolution on the shape of the  $I_{\rm H\alpha}$ – $\sigma$  diagrams. We found that the  $I_{\rm H\alpha}$ – $\sigma$  diagrams obtained after degrading the resolution not only retain its similarity in shape, but also become quantitatively close to those observed in dwarf galaxies.

ACKNOWLEDGMENTS. E.V. and Yu.S. thank the Russian Foundation for Basic Research for support (project codes Nos. 12-02-00365, 12-02-00917 and 15-02-08293). E.V. and A.M. also acknowledge the financial support from the non-profit "Dynasty" foundation. A.M. thanks for a grant from the President of the Russian Federation (MD3623.2015.2). E.V. acknowledges the Russian Scientific Foundation grant No. 14-50-00043.

#### REFERENCES

Bordalo V., Plana H., Telles E. 2009, ApJ, 696, 1668

Kaplan S. A., Pikelner S. B. 1979, Physics of the Interstellar Medium, Nauka, Moscow (in Russian)

Klingenberg Ch., Schmidt W., Waagan K. 2007, J. Comp. Phys., 227, 12

Martínez-Delgado I., Tenorio-Tagle G., Muñoz-Tuñón C., Moiseev A. V., Cairós L. M. 2007, AJ, 133, 2892

Moiseev A. V., Lozinskaya T. A. 2012, MNRAS, 423, 1831

Moiseev A. V., Pustilnik S. A., Kniazev A. Y. 2010, MNRAS, 405, 2453

Muñoz-Tuñón C., Tenorio-Tagle G., Castañeda H.O., Terlevich R. 1996, AJ, 112, 1636

Toro E. 1999, Riemann Solvers and Numerical Methods for Fluid Dynamics, Springer-Verlag, Berlin, 2nd edition

Vasiliev E. O. 2011, MNRAS, 414, 3145

Vasiliev E. O. 2012, MNRAS, 419, 3641

Vasiliev E. O. 2013, MNRAS, 431, 638

Vasiliev E. O., Nath B. B., Shchekinov Yu. A. 2015, MNRAS, 446, 1703

Yang H., Chu Y-H., Skillman E. D., Terlevich R. 1996, AJ, 112, 146